buildings

MDPI

Article

Alkali-Activated Hybrid Cement from Mineral Wool Fiber Waste and OPC

Diego A Gutiérrez-Orrego [1], Maryory A Gómez-Botero [2,*] and Edwin F García [1]

[1] School of Engineering, Grupo de Investigación en Infraestructura (GII), Universidad de Antioquia (UdeA), Calle 67 # 53-108. A. A., Medellín 1226, Colombia
[2] School of Engineering, Centro de Investigación, Innovación y Desarrollo de Materiales (CIDEMAT), Universidad de Antioquia (UdeA), Calle 67 # 53-108. A. A., Medellín 1226, Colombia
* Correspondence: maryory.gomez@udea.edu.co

Abstract: Cements to replace ordinary portland cement (OPC) are currently being studied due to the high environmental costs of OPC production. One viable alternative is alkali-activated cements, which can be made from pozzolanic materials such as stone wool fiber waste (SW). At present, SW is the most used insulation material in the world, and the disposal and recycling of it is an environmental challenge due to its fibrous nature and low density. In the present work, an alkali-activated cement (AAC) and an alkali-activated hybrid cement (AAHC) were obtained from the alkaline activation of SW. The unconfined compressive strength (UCS) of the AAC and AAHC obtained was evaluated. After 28 days of curing at room temperature, the maximum UCS reached was 6.7 MPa for samples without the addition of OPC and 12.3 MPa for those with the addition of OPC. In addition, alkaline reaction products were identified in all the combinations through XRD and SEM-EDS. The results are promising as they show a hybrid material obtained from an industrial waste product and has a reduced carbon footprint.

Keywords: alkali-activated cement; alkali-activated hybrid cement; stone wool fiber; mechanical strength; sustainable material; chemical characterization

Citation: Gutiérrez-Orrego, D.A.; Gómez-Botero, M.A.; García, E.F. Alkali-Activated Hybrid Cement from Mineral Wool Fiber Waste and OPC. *Buildings* **2023**, *13*, 354. https://doi.org/10.3390/buildings13020354

Academic Editor: Moncef L. Nehdi

Received: 9 December 2022
Revised: 5 January 2023
Accepted: 12 January 2023
Published: 27 January 2023

1. Introduction

Due to their mass use and easy application, traditional binders such as lime and cement are the most widespread stabilizing agents in civil engineering applications. However, the use of these materials has been questioned due to their high costs, not just in the economic sense but also in terms of energy and the environment [1]. For example, for each ton of ordinary Portland cement (OPC) produced, 0.99 tons of CO_2 are released, a process that represents 7–8% of the worldwide production of this greenhouse gas [2]. Faced with this problem, alternative materials have been proposed to partially replace lime and cement, such as pozzolanic materials and geopolymers, also known as alkali-activated cement (AAC). AAC are a particularly interesting option for the replacement of traditional binders. They can be obtained using fly ash, metallurgical slag, mining sludge, diatomite, and agro-industrial wastes such as rice hulls [1–3].

These materials are inorganic aluminosilicates composed of three-dimensional Si-O-Al networks, formed through polycondensation of silica tetrahedrons (SiO_2) and alumina tetrahedrons (AlO_4), that are alternately bonded and share all the oxygen atoms. Positive ions such as Na^+, K^+, Ca^{2+}, Ba^{2+}, NH^{4+}, and H_3O^+ are present in the structure's cavities, balancing the negative charge left by coordination number 4 of Al^{3+} with oxygen, and its chemical structure is in the semicrystalline to the amorphous stage [4]. The most important factors affecting alcali-activated materials, both chemically and mechanically, are the molar ratios SiO_2:Al_2O_3, R_2O:Al_2O_3, SiO_2:R_2O (R=Na^+ or K^+ generally), and the solid/liquid ratio [5]. The most important molar reactions in all species, affecting both the chemical and cementitious properties, are the molar reactions Si:Al and Na:Al [6].

The advantages of geopolymers and AAC over OPC include their high bending resistance, high compressive strength, high resistance to high temperature, high chemical resistance to chlorides and sulfates, and, above all, their multiple potential uses in combination with raw materials when derived from industrial by-products (IBPs) [7–13]. Recently, research related to the use of AAC in reinforced concrete structures such as beams [14] and ultra-high performance geopolymer concretes (UHGP) with a developed compression strength of 220 MPa [15] has been carried out. AAC can also neutralize or immobilize heavy metals and have lower energy consumption and greenhouse gas emissions than OPC [1–3,16,17].

Alkali-activated hybrid cements (AAHCs) are another material that has attracted interest [18–22]. AAHCs are cementitious binders with CaO, SiO_2, and Al_2O_3 contents of around 20%, whose reaction products are chemically complex gels, the formation of which depends on the reaction conditions. The most studied hybrid cementitious systems include OPC-blast furnace metallurgical slag, OPC-metallurgical phosphate slag, and OPC-fly ash [23]. Studies on these materials have shown that certain quantities of reactive calcium in OPC clinker allow the mixture to be set without thermal treatment. In other words, it can be set at room temperature [23–26]. These less than 30% of OPC cements are known as alkaline hybrid cements [23–27]. Recently, the use of AAHC with artificial alkali-activated aggregates has been investigated with excellent prospects for use in industry [28].

Another industrial waste that has recently drawn interest for potential use in the manufacture of alternative cements is stone wool fiber, also known as rock wool or volcanic wool. Stone wool fiber is a synthetic fiber manufactured by melting basalt rocks at high temperatures and is used for thermal insulation. Indeed, it is the most used insulating material worldwide, particularly in buildings [29]. However, due to its fibrous nature and low density, its ultimate disposal and recycling pose an environmental challenge. Based on the work by Väntsi & Kärki [30], it is estimated that 2.82 million tons of stone wool fiber will be produced in 2030 [31].

In response to the situation described above, studies have been carried out on the use of stone wool fiber waste in building materials. Due to its chemical composition (rich in SiO_2, Al_2O_3, CaO, Fe_2O_3, and MgO), amorphous nature, and high surface area, stone wool fiber shows promise for use as supplementary material in construction and as a precursor in alkali-activated cements [31]. Studies have been carried out on its use as supplementary material in concretes [32–36] and as a reinforcement material in soil-cement and blocks [37–40]. These studies reported the alkali-activation of stone wool fiber using an alkaline solution of sodium aluminate and sodium hydroxide. In the first of these studies, wool fiber waste (SW) samples and glass wool (GW) were evaluated after 28 days of curing at room temperature, along with samples cured in the same conditions but with four days of pre-treatment at 50 °C. In the second study, samples with SW and a combination of SW and fly ash (FA) were evaluated, subjecting the samples to pre-treatment at 80 °C for four days, followed by curing at room temperature for 28 days. The authors evaluated mineralogical and mechanical properties in both studies, obtaining average results of 12 and 30 MPa, respectively.

Additionally, the gels N-A-S-H and C-A-S-H were identified as reaction products. Similarly, Erofeev et al. [41] carried out alkaline activation of stone wool fiber, using an alkaline solution of sodium hydroxide and performing thermal pre-treatment. They obtained satisfactory results concerning the identification of phases associated with the formation of a geopolymer.

Meanwhile, Yliniemi et al. [42] found that the type of alkaline activator affects the kinetics and, therefore, the resistance and rapid setting. They evaluated the effect of four alkaline activators (sodium hydroxide, sodium silicate, and sodium aluminate) on the alkaline activation of SW and GW fiber at a curing temperature of 40 °C and a curing time of 28 days. These authors provided a complete description of the chemistry and structure of the reaction products of SW fiber. The main products were the amorphous gels N-A-S-H and C-(N)-A-S-H. Finally, Pavlin et al. [43] evaluated the activation of SW and GW using

sodium hydroxide and sodium silicate, individually and in combination. In this study, the compressive strength of samples cured at 40 °C for three days and at room temperature for 28 days was evaluated, finding an average compressive strength of 50 MPa.

In the present study, AAC and AAHC were obtained through the alkaline activation of SW. The AAC and AAHC obtained were evaluated by performing unconfined compressive strength (UCS) tests of samples cured at room temperature. The microstructure and morphology of the samples were analyzed through XRD and SEM-EDS. It is hoped that the results of this study will contribute to understanding the (SW)-OPC alkaline fiber system as a sustainable building material derived from industrial waste and has reduced OPC content. This could significantly contribute to the construction sector's circular economy and to the knowledge of hybrid cements systems based on SW.

2. Materials and Methods

2.1. Particle Size Distribution and Chemical Characterization of SW

The SW used for the AAC samples was taken from waste material from a company that manufactures and sells this material for insulation purposes. The SW used around 5% content of phenolic resin binder. A particle size reduction process was carried out to increase the surface area of the material, thereby increasing the effectiveness of the alkaline activation. This reduction was made using ceramic alumina ball mills until a particle size was reached that passed through the # 14 sieve (ASTM sieve) with a 1.40 mm opening. Grinding was performed at a speed of 71.3 rpm, for 15 minutes, with mineral wool loads between 100 and 200 g. The average density of the fiber is 1.40 kg/m^3, specific gravity of 1.12 g/cm^3 and thermal conductivity 0.036 W/(m.ºK). Pictures of the SW and the milling process are shown in Figure 1. Meanwhile, the cement (OPC) used in the study was a grey general-use cement that complies with the specifications of the Colombian Technical Standards NTC 121 [44], which is analogous to ASTM C1157 [45], used in this work. The physical properties of the cement are presented in Table 1.

Table 1. Standard physical requirements of cement of general use (OPC).

General Construction Cement Type	Value
Fineness (cm^2/g)	Minimum 2.800
Autoclave length change (%)	0.8
Air content of mortar volume (%)	Maximum 12
Mortar bar expansion—14 days (%)	0.02

The particle size distribution of the milled SW fiber was determined using the laser diffraction method. The device used for this was a Master Sizer 2000 Single Narrow model, while an aqueous solution of sodium hexametaphosphate at a concentration of 40 g/L was used as a dispersant. Subsequently, chemical characterization of the fiber was performed using XRD, XRF, and SEM-EDS to identify its chemical composition and microstructural morphology.

Similarly, XRF was performed on the OPC cement to identify its chemical composition. For the XRF of both materials, an AxiomAX Minerals device by Panalytical was used, following the fused beads procedure and using semi-quantitative software. For the XRD analysis, the pulverized fiber sample was passed through the # 100 sieve (ASTM sieve), and the analysis was then performed using an Empyream-Panalytical diffractometer with copper radiation source [Cu, K α = 0.1541 nm (1.541 Å)], in a range of 2θ between 5 and 80° and a sweep of 0.0263°. For the SEM-EDS, a JEOL-JSM-6490-LV device was used, loading the sample on a graphite ribbon before applying a thin gold (Au) coating in a DENTON-VACUUM Desk IV device.

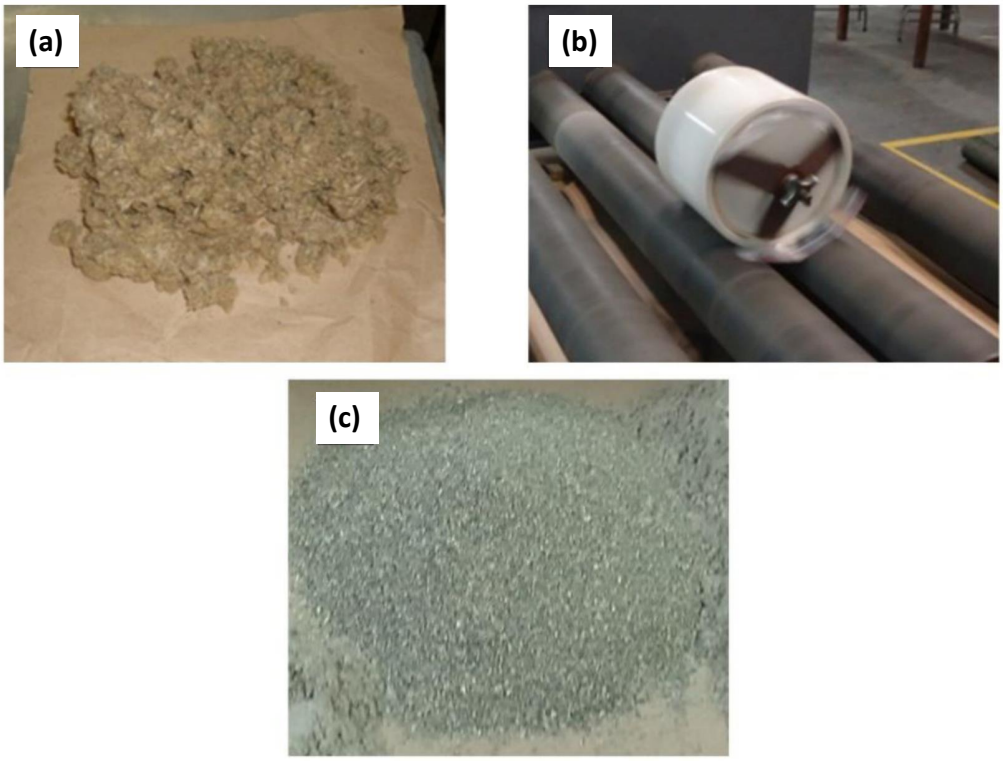

Figure 1. Pictures of the SW. (**a**) SW fiber, (**b**) Ball milling process and (**c**) SW after the milling process.

2.2. Design of Experiments Description

The design experiments carried out were a completely randomized factorial design. The design was fixed and balanced. The factorial structure was $3 \times 3 = 3^2$ (two factors, three levels). The design was made with three replicas, with 27 runs or experimental units. The first factor (type of alkaline activator) was fixed at three levels, i.e., varying the concentrations of sodium hydroxide (NaOH) and sodium aluminate ($NaAlO_2$) in the activator to reach three molar ratios of Na:Al (1.2, 1.8 and 2.2), while keeping the Si:Al ratio fixed (Si:Al = 1.9); these values were taken from range values in previous works [6,46]. The second factor (OPC percentage) was fixed at three levels, which were 0, 15, and 30% in weight percent concerning the total weight of the mixture. The response variable was UCS, which was determined by failing the samples after 28 days of curing. After obtaining the data, an ANOVA analysis (Two-way ANOVA) and a comparison of treatment means by Tukey's method were performed to statistically determine the effect of the type of alkaline activator on the UCS of the samples without and with the addition of 15 and 30% OPC. A proposed second-order model determines a relationship between the input variable (activator-OPC) and the response variable (UCS) of the alkali-activated OPC-fiber system based on the data. The design of experiments was performed using R Studio software version 1.2.1578.

2.3. Surface Response of AAC and AAHC

A second order model (Equation (1)) is proposed, that determines a relationship between the input variable (activator-OPC) and the response variable (UCS) of the alkali-activated OPC-fiber system based on the data found in the designed program. This model aims to illustrate a surface response graphically to visualize the optimal region. A two-factor quadratic or second-order model can be written as follows:

$$Y = \beta_0 + \beta_1 X_1 + \beta_2 X_2 + \beta_{11} X_1^2 + \beta_{22} X_2^2 + \beta_{12} X_1^2 X_2^2 + \epsilon \quad (1)$$

where Y is the response variable, x_1 y x_2 are the factors, and ϵ is the experimental random error effect.

2.4. Preparation of the Alkaline Solutions

The chemical variable sought to control among the three alkaline solutions was the molar ratio Na:Al, keeping the molar ratio Si:Al fixed. Therefore, in the three alkaline activator solutions, the molar ratio Na:Al was varied (1.3, 1.8, and 2.2), while the Si:Al ratio was kept constant at 1.9. Of the molar units or ratios, these last two substantially influence alkali-activated cements' physical and mechanical properties [6,47,48]. Similarly, the Solid/Liquid ratio was kept constant for all the mixtures, as were the Water/(Fiber+OPC) ratios for the different levels of each activator mix. The additions, in grams and milliliters, of the component of AAC samples, as well as the molar and Solid/Liquid ratios, are shown in Table 2.

Table 2. Summary of dosages in grams and milliliters of alkali-activated cement.

Mixture	SW (g)	OPC (g)	Activat. Solution (g)	Added Water (mL)	Total Water-W (mL)	S:L *	Si:Al	Na:Al	W/(SW + OPC)
Act.1—0%	46.0	0.0	50.7	1.0	31.4	0.91	1.9	1.3	0.68
Act.1—15%	46.0	8.1	50.7	0.0	31.4	0.91	1.9	1.3	0.58
Act.1—30%	46.0	19.7	50.7	2.0	33.4	0.91	1.9	1.3	0.51
Act.2—0%	47.0	0.0	52.0	2.5	31.9	0.90	1.9	1.8	0.68
Act.2—15%	47.0	8.3	52.0	2.5	31.9	0.90	1.9	1.8	0.58
Act.2—30%	47.0	20.1	52.0	5.0	34.4	0.90	1.9	1.8	0.51
Act.3—0%	47.0	0.0	52.0	4.5	31.8	0.90	1.9	2.2	0.68
Act.3—15%	47.0	8.3	52.0	5.0	31.8	0.90	1.9	2.2	0.58
Act.3—30%	47.0	20.1	52.0	7.0	34.3	0.90	1.9	2.2	0.51

* The S:L ratio is calculated from the grams of SW and the grams of the activator solution.

The preparation of NaOH and Na-aluminate mixtures we prepared as follows; for activator 1 (Act.1), it was prepared a NaOH solution to 6.7 M; for activator 2 (Act.2) to 12 M; and for activator 3 (Act.3) to 16 M. Subsequently, each NaOH solution was mixed with a sodium aluminate solution (Al_2O_3 23% by weight, Na_2O 19% by weight). Then, each solution was diluted in water until the activator solution was reached, as listed in Table 2.

After preparation, each solution was left to rest for 24 hours and then mixed with the fiber until the chemical balance was reached. Finally, the pH of the three activators (NaOH and Na-aluminate mixtures) solutions was determined using a pH meter, finding a pH for each of approximately 13.0.

2.5. Preparation of Cylindrical Samples, USC Assay and Chemical Characterization Conditions for the AAC Samples

Cylindrica samples of AAHC were made to perform unconfined compressive strength tests. The samples had dimensions of 16 mm diameter and 32 mm height, seeking a diameter/height ratio of 1:2 (Figure 2). For the mixtures without added cement (AAC), the first step in creating the samples was adding the alkaline solution to the ground fiber and manually mixing it until it was homogenized. Subsequently, water was added to adjust the Water/SW (W/SW) ratios, and manual mixing was carried out until homogenization was again reached. For the mixtures with added fiber and OPC (AAHC), the dry fiber and cement were manually mixed before adding the alkaline solution and the fiber to adjust the W/(SW + OPC) ratio and then mixing again until homogenization. The mixing process lasted between 10 and 20 min.

Figure 2. Alkali-activated stone wool fiber specimens with and without OPC addition.

Once homogenization was achieved, the mixture was placed into cylindrical PVC molds. After four days, they were removed from the molds and cured for 28 days. The reason for leaving the mixtures in the molds during this period was that they did not meet the necessary consistency in the demolding process and were damaged or deformed when removed before four days had elapsed. After demolding, the samples were put in a humidity chamber. The curing conditions of the samples were average temperature of 23(±2) °C and relative humidity (RH) of 99(±1)%. The UCS tests of the cylindrical samples were carried out in a Shimadzu series AGX device with a load of 5 kN and a load velocity of 2.4 kN/s.

Once the cylindrical AAC samples failed, a sample of each combination was extracted from the failure zone and subjected to XRD and SEM-EDS to carry out chemical characterization, find phases associated with the formation of geopolymers and obtain information on the morphology of the samples. For the XRD analysis, it followed the same procedure indicated previously for the fiber. However, Rietveld analysis was not conducted to determine the amorphous phases of the alkali-activated material. The ICSD database (Inorganic Crystal Structure Database, [49]) was used for phase identification. The SEM-EDS was carried out using the previously mentioned device, and the samples were prepared with the stone wool as previously described.

3. Results and Discussion

3.1. Raw Material Characteristics

The particle size distribution of the SW is shown in Figure 3, where a bimodal distribution (two peaks) can be observed between 0.50 µm and 1120 µm, which are the sizes with the highest frequency. The first is 20 µm, and the second is 100 µm. The assay also found a d(0.5) of 53.224 µm.

Although SW, compared to other insulation materials, has a lower environmental impact in terms of life cycle energy consumption [29], its disposal at the end of its life cycle is of concern due to its deficient post-consumer related to technical, economic and health problems [50]. Among the size reduction methods for stone wool fiber, the ball mills method is an effective method for bulk density and particle size reduction. It is recommended as a feasible method to be scaled up to the industrial level [50]. Therefore, this method can be used at the industrial level to produce AAC materials, with lower energy consumption in waste shredding and, consequently, a lower environmental impact.

The XRF results in Table 3 show SiO_2 as the oxide component with the highest percentage in the SW, followed by CaO Al_2O_3, MgO, and Fe_2O_3. Meanwhile, the main component for OPC was CaO, followed by SiO_2, Al_2O_3, and Fe_2O_3. In Figure 4, the SEM images of the ground fiber are shown, while Figure 5 shows the EDS results obtained from the fiber. In Figure 4, approximate fiber diameters between 2.98 and 17.77 µm and approximate lengths between 20 and 80 µm can be seen per the particle size ranges shown in Figure 3. Meanwhile, a smooth morphology of the fiber can be observed, with small particles adhering to its surface, possibly of the same material as the fiber. Similarly, in Figure 5, it can be observed that, according to the EDS spectra carried out on the fiber's surface, its

chemical composition consists mainly of Si, Ca, Al, Mg, Fe, Na, and Ti. This chemical element distribution follows the XRF analysis shown in Table 3. As for ignition losses (LOI at 950 °C), the OPC showed a loss of 5.2%, while a sample of SW without the phenolic resin binder showed no loss.

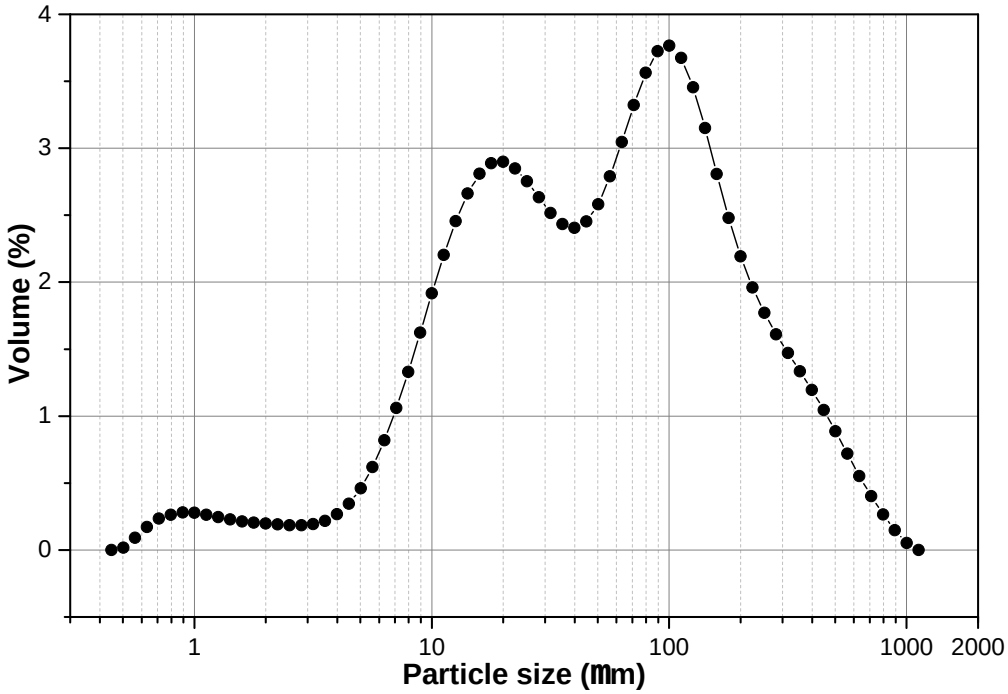

Figure 3. Particle size distribution of stone wool fiber by Laser Beam Diffraction (LRD).

Table 3. Chemical composition of the SW and the OPC (%) by X-ray Fluorescence.

Comp.	SiO_2	Al_2O_3	Fe_2O_3	TiO_2	CaO	MgO	Na_2O	K_2O	MnO	P_2O_5	SO_3
SW	45.56	12.53	6.8	0.88	21.61	10.43	1.57	0.15	0.17	0.1	0.07
OPC	27.6	7.58	2.85	0.4	49.1	1.77	0.25	1.16	0.89	0.43	2.62

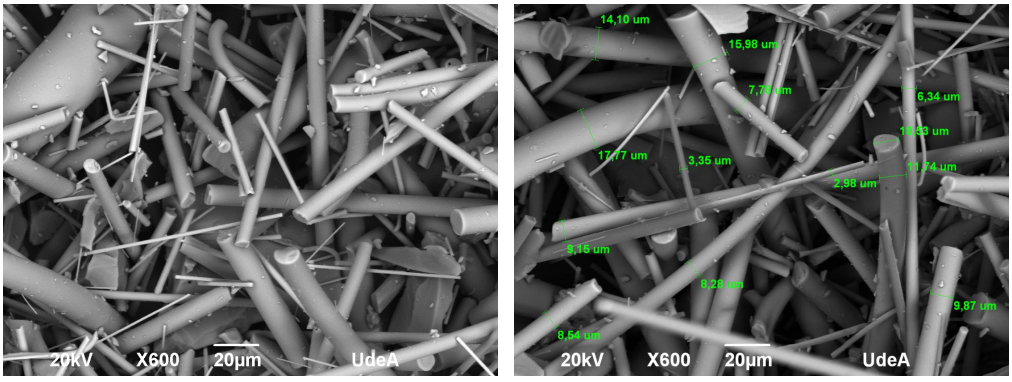

Figure 4. SEM images of the stone wool fiber after the grinding process.

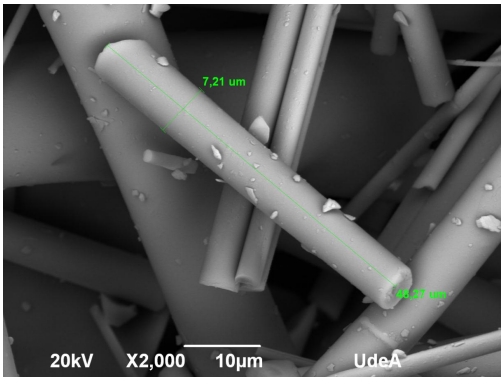

Element	App Conc.	Intensity Corrn.	Weight%	Weight% Sigma	Atomic%
O K	48.44	0.5463	34.10	0.54	50.42
Na K	2.36	0.8160	1.11	0.12	1.15
Mg K	13.53	0.7555	6.89	0.14	6.70
Al K	14.99	0.7824	7.37	0.14	6.46
Si K	53.99	0.8006	25.94	0.27	21.85
Ca K	45.11	0.9747	17.80	0.21	10.51
Ti K	1.17	0.7871	0.57	0.09	0.28
Fe K	13.45	0.8309	6.23	0.18	2.64
Totals			100.00		

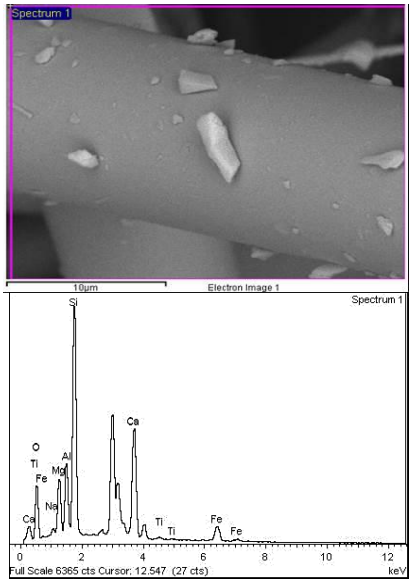

Figure 5. EDS analysis of milled stone wool fiber.

3.2. Unconfined Compressive Strength (UCS) of the AAC and AAHC Samples

Figure 6 shows the UCS results for the nine grouped combinations, with the levels of OPC percentage and W/(SW+OPC) ratio. As shown in Figure 6, the highest UCS, of 12.35 MPa, was achieved for the Act.2—15% mixture corresponding to the AAHC samples, followed by the Act.1—15% mixture at 10.50 MPa. Of the AAC samples, the highest strength, at 6.62 MPa, was achieved with the Act.2—0% mixture, followed by the Act.3—0%, with 4.18 MPa. The highest strength values were obtained at the 15% OPC level for Act.1 and Act.2, while with Act.3, they were obtained at a 30% OPC level. Similarly, the strength tended to increase from Act.1 to Act.2 before decreasing when passing to Act.3, independently of the OPC level. This suggests a synergy in the reactions when OPC is combined with the alkaline activators Act.1, Act.2, and the SW.

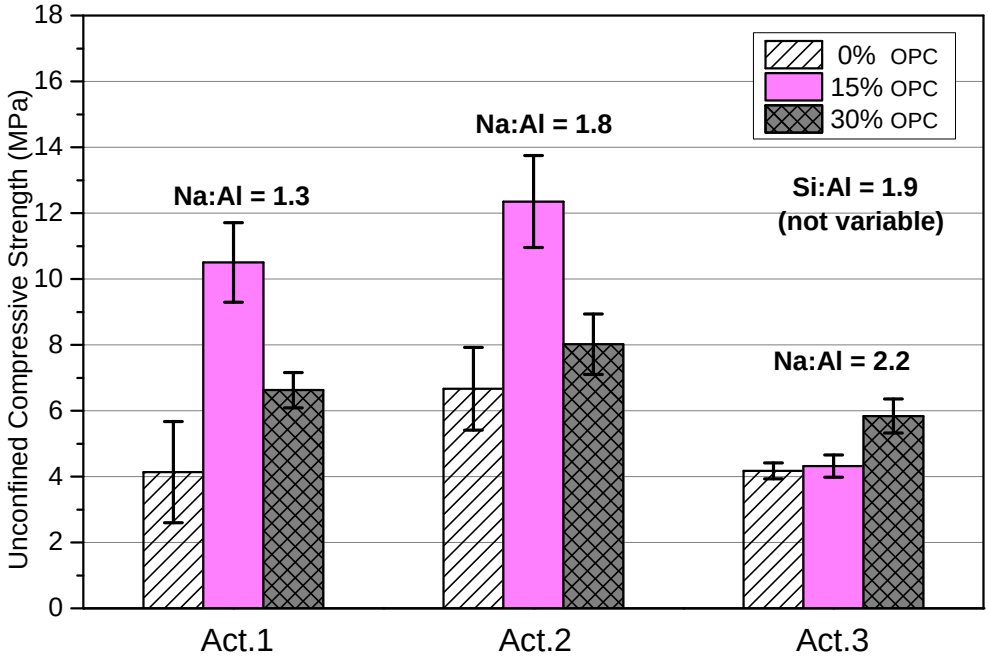

Figure 6. UCS vs. Activator (Act.) bar graph of alkali-activated cement (AAC).

Yliniemi et al. [42] reported that using sodium aluminate kinetically retards the SW reaction when compared with using sodium hydroxide and sodium silicate. These authors conducted calorimetric studies using a 40 °C isotherm. In the present work, a combination of sodium aluminate and sodium hydroxide was used at room temperature. This could explain the prolonged time required, of four days, for the setting of the AAC samples to be visually apparent.

Some works have studied the effect of adding OPC in alkali-activated materials. For instance, Garcia-Lodeiro et al. [23] and Palomo et al. [51] reported that in systems containing fly ash (FA) in proportions of 30% OPC–70% FA, the addition of OPC accelerated the alkaline activation of the fly ash at room temperature. This acceleration is caused by the energy released by the OPC during the hydration process in the form of heat, which in turn causes the activation of chemical reactions that result in the setting and hardening of the fly ash in a highly alkaline material. Moreover, these authors add that the hydration of OPC in these systems depends on the concentration of OH and the presence of soluble silicate in the medium.

Similarly, Angulo–Ramírez et al. [52] evaluated OPC + GBFS (granulated blast furnace slag 80%) mixtures through calorimetric assays, varying the combinations of the sodium silicate and sodium hydroxide activator. Their results showed that the heat released by these alkali-activated systems is much greater than if they had been hydrated with water but much lower than a mixture of 100% OPC. In addition, they concluded that the type of activator influences the reaction kinetics, especially at the early stages. The same conclusion was reached by Garcia-Loderio et al. [25] when they evaluated a cement hybrid of 70% FA–30% OPC.

In the present work, the AAC samples containing OPC (15 and 30%) were set more quickly than the samples that did not contain OPC (0%). OPC probably accelerates the setting and hardening of the matrix, as is the case in OPC + FA and OPC + GBFS in highly alkaline media.

Additionally, some studies have evaluated sodium aluminate ($NaAlO_2$) as an accelerator in the hydration processes of special OPC cement in low-temperature conditions. Lota et al. [53] showed that the hydration of a special cement in aqueous solutions of 0.1 to 1 M $NaAlO_2$ is accelerated as the solution forms hydration confining shell that completely covers the cement grains. Moreover, the Al ions originating from the sodium aluminate react rapidly with the Ca ions released due to the dissolution of the calcium silicates of the cement, thereby forming hydrated calcium aluminates. Similarly, Andersen et al. [54] found that sodium aluminate accelerates the hydration of the alite and belite in white OPC in a temperature range between 5 and 20 °C.

Based on the above, using sodium aluminate ($NaAlO_2$) as an alkaline activator may have favored the acceleration of the hydration processes of OPC and, in turn, the alkaline activation of the SW by releasing hydration heat and thereby accelerating the setting process.

3.3. ANOVA Analysis and Comparison of Treatment Means

Figure 7a shows a similarity and greater dispersion of data in the activating solutions Act.1 (Na:Al=1.3) and Act.2 (Na:Al = 1.8), concerning Act.3 (Na:Al = 2.2). Likewise, Figure 7b shows that the 15% OPC level has the mean and median above the 0 and 30% OPC levels, but it is the level with the greatest dispersion. It can also be seen that there is a slight increase in UCS from 0 to 30% levels, but it is not clear if there is a significant difference between them. Finally, at the 0% and 30% levels, some "outlier" points appear; however, the data meet the assumption of normality and, therefore, will not affect the estimation parameters.

Table 4 shows the results of the ANOVA analysis of the factorial design of the AAC and AAHC specimens. Table 4 shows that the *p*-value is much lower than 0.05 (95% confidence level), both for Act, OPC, and their interaction (Act:OPC), which indicates the null hypothesis of equality in the mean of the treatments can be rejected. This result confirms the synergy between the activating factor and the OPC factor. According to the ANOVA

analysis, Table 5 presents Tukey's method results between Act.1 and Act.2. with their respective OPC levels (treatments pairs comparison), as they presented the highest average UCS resistances, according to Figure 6.

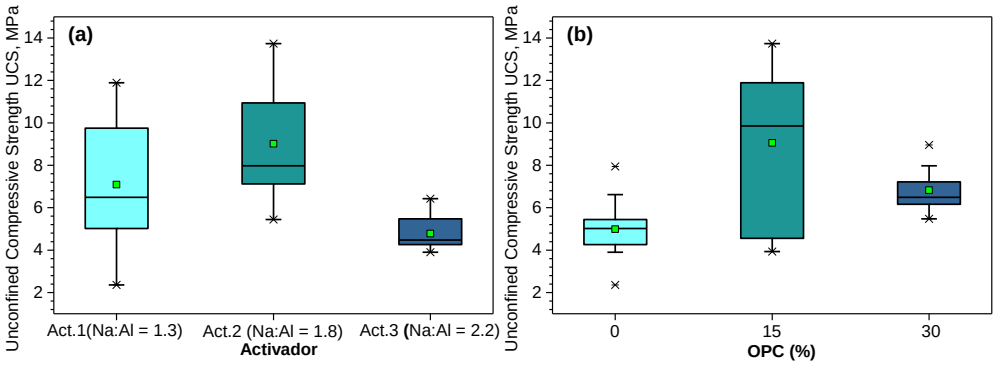

Figure 7. Box and whiskers plot: (**a**) UCS vs. Activator and (**b**) UCS vs. % OPC.

Table 4. Two-way ANOVA results factorial design.

	Degree of Freedom	Sum of Squares	Mean Square	F-Value	*p*-Value
Activator	2	80.9	40.45	40.86	2.03×10^{-7}
OPC	2	74.61	37.3	37.68	3.68×10^{-7}
Act:OPC	4	45.17	11.29	11.41	8.65×10^{-5}
Residuals	18	17.82	0.99		

In Table 5, for all treatment pairs between Act.1 and Act.2, at the 0, 15, and 30% OPC levels, the *p*-value is greater than 0.05. Additionally, for all three levels of activator and percentage of OPC, the confidence interval range (95%) includes 0. Therefore, the results suggest that the null hypothesis between the treatment means cannot be rejected for the three pairs of treatments compared. No significant difference in UCS response is found between Act.1 (Na:Al = 1.3) and Act.2 (Na:Al = 1.8), independent of the percentage level of OPC.

Table 5. Tukey's method results between Act.1 and Act.2. with their respective OPC levels. C.I. (95%).

Treatments Pairs	Difference	Lower Bound	Upper Bound	Adjusted *p*-Value
Act.1—0% OPC : Act.2—0% OPC	2.53	−0.31	5.34	0.10
Act.1—15% OPC : Act.2—15% OPC	1.85	−0.99	4.70	0.42
Act.1—30% OPC : Act.2—30% OPC	1.40	−1.50	4.24	0.73

3.4. Quadratic Model Experiment with AAC and AAHC

The quadratic equation (Equation (2)), following the coefficients found by the R software, is presented below. Also, Table 6 shows a summary of the model's parameters.

$$R = 11.07 - 1.154 * Act + 0.919 * OPC - 0.206 * Act * OPC - 3.081 * Act_2 - 3.147 * OPC^2 \quad (2)$$

where:
R = UCS, in MPa.

Act = Na:Al ratio of the alkaline activator, at a constant Si:Al ratio (1.9).
OPC = Percentage of OPC.

Table 6. Summary quadratic model alkaline-activated cement.

	Degrees of Freedom	F-Value	*p*-Value
Quadratic model	5	10.49	3.76×10^{-5}
Coefficient of determination R^2	0.7141		
Adjusted coefficient of determination $R^2{}_{adj}$	0.646		

As seen in Table 6, the model is significant considering the *p*-value, which is much lower than the significance level of 0.05. Also, it shows that the R^2 is 0.7141, which means that around 71.41% of the variability of the UCS is explained by the model, which is an acceptable value. Afterward, the $R^2{}_{adj}$ is shown, with a value of 0.646. The fact that the $R^2{}_{adj}$ drops concerning R^2 indicates that there are terms within the model that do not contribute significantly. For prediction purposes, it is recommended that R^2 be adjusted to at least 0.70 [55]. In this case, the R^2-value is approximately at that level.

Figure 8a shows the contour map graph, while Figure 8b shows the surface response of the quadratic equation mentioned. It can be observed in Figure 8a that the region that includes the maximum UCS values is located between the Act. values: 1.6–1.8, and OPC: 15–20%, approximately. Additionally, Figure 8b shows that the maximum surface response value corresponds to the domain region or contour map described previously. Although it is sensitive to the lack of adjustment, it is considered that this model can graphically represent an approximation of the behavior of the response variable (UCS) relative to the activators and OPC factors based on the UCS results.

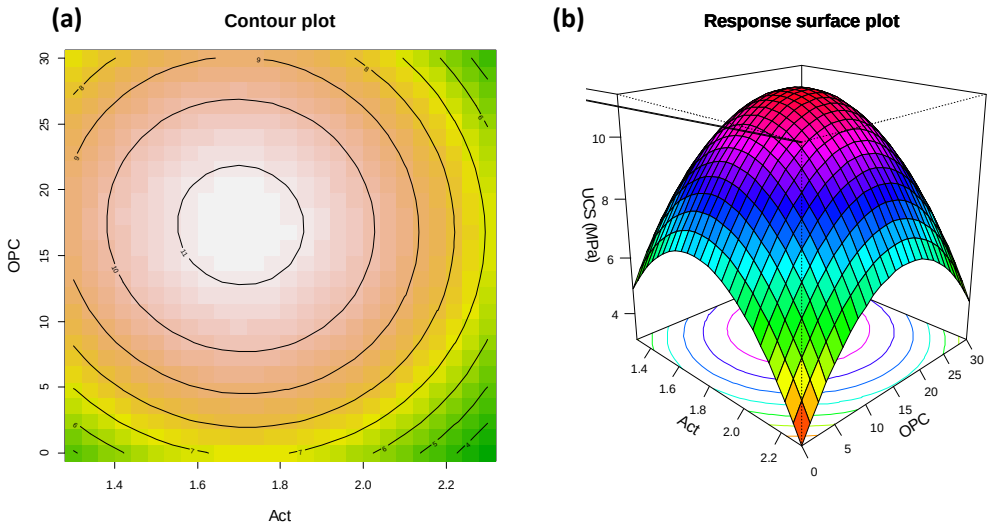

Figure 8. Results of the quadratic model: (**a**) AAHC contour map; (**b**) AAHC response surface plot.

3.5. X-ray Diffraction (XRD)

Figures 9–11 show the x-ray diffraction results on the nine samples of combinations of alkali-activated cements, including both AAC and AAHC samples. According to the three activators, these results have been grouped into three figures. The three activators consist of Act.1 (Na:Al = 1.3), corresponding to Figure 9; Act.2 (Na:Al = 1.8) corresponding to Figure 10; and Act.3 (Na:Al = 2.2) corresponding to Figure 11. Each group's combination is shown with its respective OPC level (0–15–30%). Additionally, they are compared with the diffractogram of the inactivated stone wool (denoted as "Fiber") to analyze the changes in the AAC and AAHC samples.

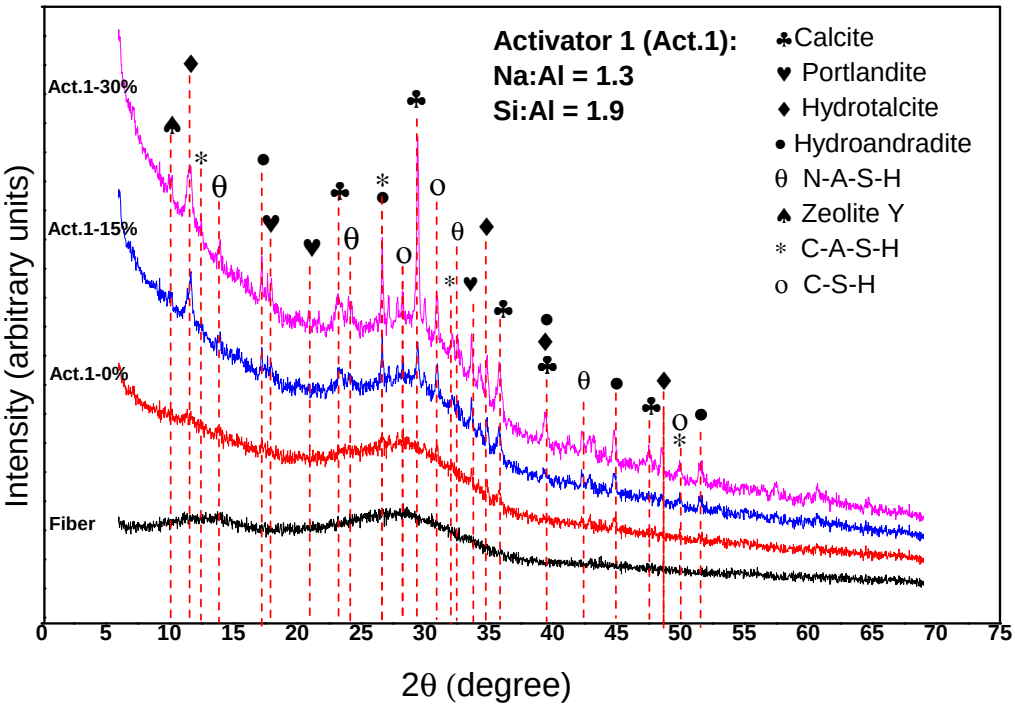

Figure 9. Diffractograms (XRD) of the combinations of alkali-activated cement with Act.1, without addition and with the addition of OPC.

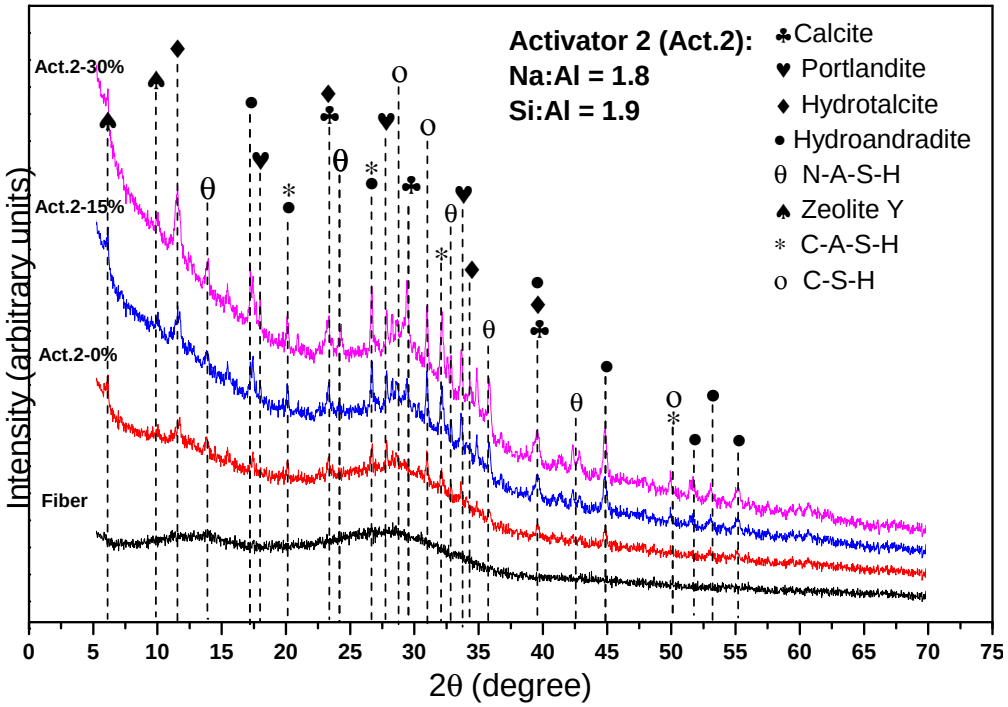

Figure 10. Diffractograms (XRD) of the combinations of alkali-activated cement with Act. 2, without addition and with the addition of OPC.

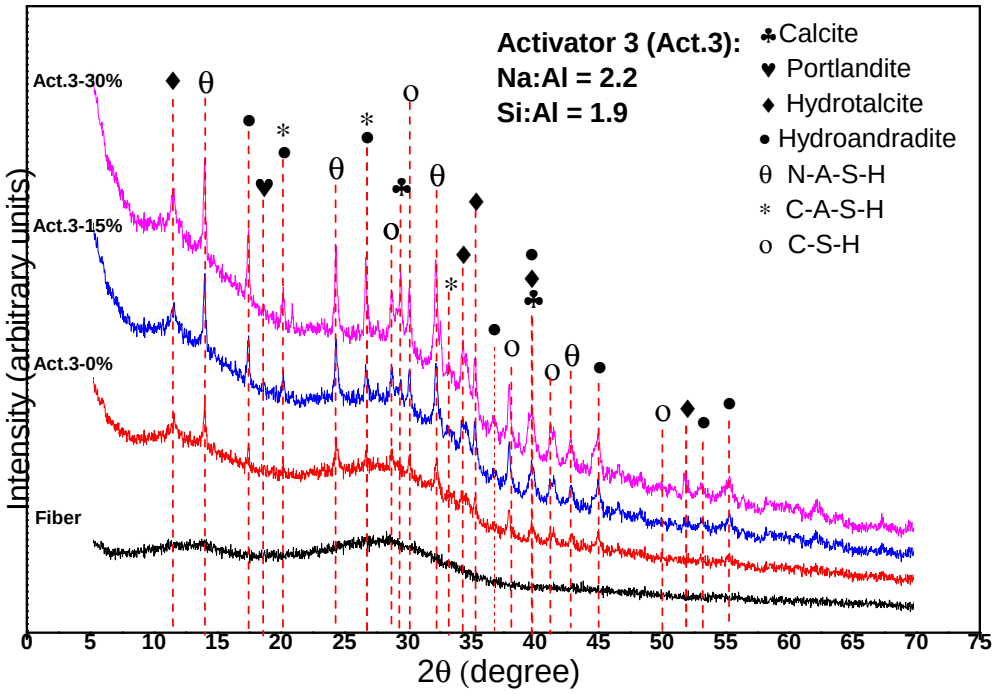

Figure 11. Diffractograms (XRD) of the combinations of alkali-activated cement with Act.3, without addition and with addition of OPC.

The phases identified were: hydrotalcite, $((Mg_4Al_2)(OH)_{12}(CO_3)(H_2O)_3)_{0.5}$: Powder Diffraction File (PDF) #00-014-0191; hydroandradite, $Ca_3Fe_2(SiO_4)_{1.15}(OH)_{7.4}$: (PDF) #01-075-0553; Y-type zeolite, $Na_3H_{53}Al_{56}Si_{136}O_{384}$: (PDF) #00-038-0239; sodium alumina-silicate hydrate, N-A-S-H: (PDF) #00-041-0009; calcium alumina-silicate hydrate C-A-S-H (PDF) #00-033-0306; calcium silicate hydrate, I-type C-S-H: (PDF) #00-034-0002; portlandite $Ca(OH)_2$: (PDF) #00-004-0733 and calcite, $CaCO_3$: (PDF) #00-013-0135. All these phases were found in each of the three types of AAC, except for the Y-type zeolite, whose characteristic peaks were identified in the AAC with Act.2 (Figure 10) but could only be seen slightly in the AAC with Act.1 (Figure 9) and could not be seen in the AAC with Act.3 (Figure 11).

The fiber without alkaline activation presents an amorphous structure with two broad bands between the angles 2θ:10–15° and 20–35°, approximately. Meanwhile, in the nine combinations with alkaline activation, the shape of these bands is different from the inactivated fiber, while the formation of some crystalline phases with very good intensity is observed with the addition of OPC. The change in the shifting and the shape of the bands in an amorphous structure in materials rich in aluminosilicates can indicate the formation of zeolite nanocrystals [56]. This change in the shifting of the bands in alkali-activated SW was also found by Yliniemi et al. [38] and Kinnunen et al. [40], who reported the formation of geopolymer phases.

The phases associated with the formation of a alkali-activated material that was identified were the gels N-A-S-H (sodium alumina-silicate hydrate) and C-A-S-H (calcium alumina-silicate hydrate). The C-S-H type I phase identified has also been found in an alkali-activated stone wool system, as reported by Erofeev et al. [41]. The gel N-A-S-H is known to be the main alkaline reaction product in alkali-activated cement systems, while the gel C-(A)-S-H is the main binding phase of OPC [24]. Additionally, the N-A-S-H gel's formation mechanisms and chemical structure are substantially different from that of the C-S-H gel produced by the hydration of OPC [25,57].

Following these XRD results, the identification of the Y-type zeolite in the AAC with Act.2 suggests a more significant development of the N-A-S-H gel, given that Y-type zeolite is known to be a secondary reaction product of alkali-activated cement systems [23].

Therefore, the superior mechanical strength achieved for AAC-Act.2 and AAHC-Act.2 could be attributed to the greater development of N-A-S-H and Y-type zeolite, as shown in Figure 10. The formation of the N-A-S-H gel improves the mechanical strength of the alkali-activated material because this gel fills the porosity and eventual cracks that may form during hardening, generating more compact cement and, therefore, with improved mechanical properties. In addition, authors have found that the formation of the N-A-S-H gel leads to more ordered structures increasing the crystallinity [58].

Some studies have investigated the co-precipitation of C-S-H and N-A-S-H gels in alkali-activated systems using FA as a precursor [23–25,57,59]. These results have shown that, in the presence of Ca^{2+} and Al^{3+} and at pH greater than 12, C-S-H gel and N-A-S-H gel are converted to the gels C-A-S-H and (N,C)-A-S-H (aluminosilicate with partial substitution of sodium and calcium), respectively. These last two gels have a three-dimensional structure with a relatively high degree of polymerization and crosslinking of Si [22]. Moreover, it has been found that the N-A-S-H gel, when stable at low pH, behaves like a zeolite and exhibits ion exchange behavior in which Ca displaces Na until the available Ca within the medium is exhausted. According to this, the identification of the Y-type zeolite would indicate a higher development of the (N,C)-A-S-H gel which has a higher degree of polymerization and higher Si crosslinking. Therefore, a higher mechanical performance would be obtained [24].

Garcia-Lodeiro et al. [57] propose a nanostructural model of the formation of gels in AAHCs. According to this model, the gels C-S-H and N-A-S-H are simultaneously precipitated after dissolution until saturation of the dissolved species of aluminosilicate and calcium silicate in the alkaline medium is reached. In this process, the two gels compete for the absorption of Si that originates in an early form from the calcium silicate of the OPC. In parallel to this process, the Ca^{2+} and Al^{3+} ions present in the aqueous solution begin to diffuse through the hardened cementitious matrix, and some of the Ca^{2+} ions that are not taken by the C-S-H interact with the N-A-S-H gel to form the (N,C)A-S-H gel, where their three-dimensional structure is conserved. In the presence of high concentrations of Al^{3+}, C-S-H is absorbed in the gels' bonding sites, forming C-(A)-S-H. As the concentration of Al^{3+} increases, C-A-S-H is formed [20]. Meanwhile, the OH:AI ratio in the activator solution can also be vital in understanding the formation of these phases. Depending on the OH:Al ratio, the dissolved aluminum can contain 4 or 6 coordination numbers, affecting the formation of the aluminosilicate phases [59].

Given the above, the AAC and AAHC systems were kept in an alkaline state (pH = 13) for the Ca^{2+} and Al^{3+} ions to interact in the cementitious matrix. Additionally, as there was a greater presence of the Al^{3+} ion due to the combined use of sodium aluminate and sodium hydroxide as an activator, the formation of C-A-S-H gel was favored over that of the N-A-S-H gel. With the addition of OPC (AAHC system), the processes leading to forming the reaction products mainly identified in the AAC system were accelerated. This is reflected in the more excellent crystallinity in all the AAHC combinations, which can be observed in the XRD results shown in Figures 9–11.

Meanwhile, it is possible that the formation of the N-A-S-H and (N C)-A-S-H gels was favored by the addition of OPC in the AAHC-Act.1 and AAHC-Act.2 combinations. This is particularly likely with the 15% OPC level, which resulted in greater development of UCS. Indeed, in all the AAHC combinations, increasing the level of OPC (15% and 30%) resulted in excess Ca^{2+} in the system. This could have led to a greater development of C-A-S-H gel than of N-A-S-H and (N C)-A-S-H gels, which would, in turn, lead to a lower UCS, as can be seen in Figures 6 and 7b. However, an excess of the Ca^{2+} ion in the system, with the addition of OPC at a level of 30%, would cause a reduction in UCS.

N-A-S-H gel constantly interacts with Ca^{2+} due to the strongly polarizing effect of Ca^{2+}, which distorts the Si-O-Al bonds, leading to forces that result in the breakage and reorganization of a new polymeric structure in which Si-O-Ca type bonds are formed. This, in turn, results in the conversion of N-A-S-H to (N C)-N-A-S-H and, finally, to C-A-S-H, provided there is sufficient Ca^{2+} for this last gel to be formed [25]. The prevalence

of C-A-S-H gel over N-A-S-H gel explained the reduction in UCS when 30% OPC was used for all the activators, in particular for Act.1 and Act.2 (see Figure 6), given that the development of this last gel is responsible for the increase in resistance in the alkali-activated cements [58].

About the hydrotalcite phase ($(Mg_4Al_2)(OH)_{12}(CO_3)(H_2O)_3)_{0.5}$, which is also known as quintinite and belongs to the layered-double hydroxides (LDHs) [42], this has been observed together with the formation of geopolymer structures where SW was activated [38,41,42]. This phase is formed due to the high level of MgO provided by the fiber and its exposure to the atmosphere (CO_2). This phase co-exists stably with the principal reaction product (C-(N)-A-S-H) in alkali-activated SW. It could be a control parameter in the reaction kinetics in AAC. None of the studies related this phase to the increase in the strength of the samples.

Concerning the hydroandradite phase ($Ca_3Fe_2(SiO_4)_{1.15}(OH)_{7.4}$), in the previous studies of alkaline activation of SW known to the authors, this has not been identified. It makes its identification in the current study a novel finding. The formation of this phase could be associated with the high CaO content (21.6%), as well as the Fe_2O_3 content (6.8%) present in this fiber in its natural state (see Table 3). Additionally, it has not been suggested by the authors of the studies that both MgO and Fe_2O_3 take part in geopolymer reactions. SW presents contents of these oxides that are higher than the unit (10.4 and 6.8%, respectively), as can be observed in the XRF results for the fiber shown in Table 3.

Finally, about the calcite or calcium carbonate ($CaCO_3$) phases and the portlandite or calcium hydroxide $Ca(OH)_2$, identified in both the AAC and AAHC samples, it has been reported that these materials are more susceptible to carbonation than OPC mortars, despite the microstructure of AAHC being more compact and less permeable than that of AAC. This behavior could be explained by the fact that there was not sufficient $Ca(OH)_2$ to neutralize CO_2. Therefore, the C-S-H gel reacts with the CO_2, causing the disintegration of the C-A-S-H gel due to decalcification, resulting in superficial carbonation in the material [22].

3.6. Scanning Electron Microscopy (SEM) and Energy-Dispersive X-ray Spectroscopy (SEM-EDS)

The following are the results of the scanning electron microscopy (SEM) and energy-dispersive X-ray spectroscopy (SEM-EDS) assays carried out on the AAC and AAHC samples after 28 days of curing and failing compressive strength tests. The SEM images compare the AAC samples with the three activators (Act.1, Act.2, and Act.3) and different OPC levels (0–15–30%). Concerning the EDS results, the activators Act.1 and Act.3 at 0 and 30% OPC are compared to identify and analyze the differences in chemical composition between the mixtures with the most significant differences in alkali activators (Act.1 and Act.3) and OPC percentage (0 and 30%).

In the first two images (a and b) in Figures 12–14, corresponding to the AAC, reaction products can be observed adhering to the surface due to the alkaline activation of the SW. This shows that new alkaline reaction products have been formed independently of the variation in the alkaline activator's molar ratio (Na:Al). Meanwhile, comparing the SEM images (c and d) corresponding to AAHC, reaction products can also be seen on the surface of the fiber, especially in Figures 12c and 13c; showing a rougher surface morphology of the fiber. Also, in Figures 12d and 14c, a morphology associated with the formation of reaction products can be observed, specifically the formation of N-A-S-H and C-A-S-H gels, as has also been reported by Kinnunen et al. [40].

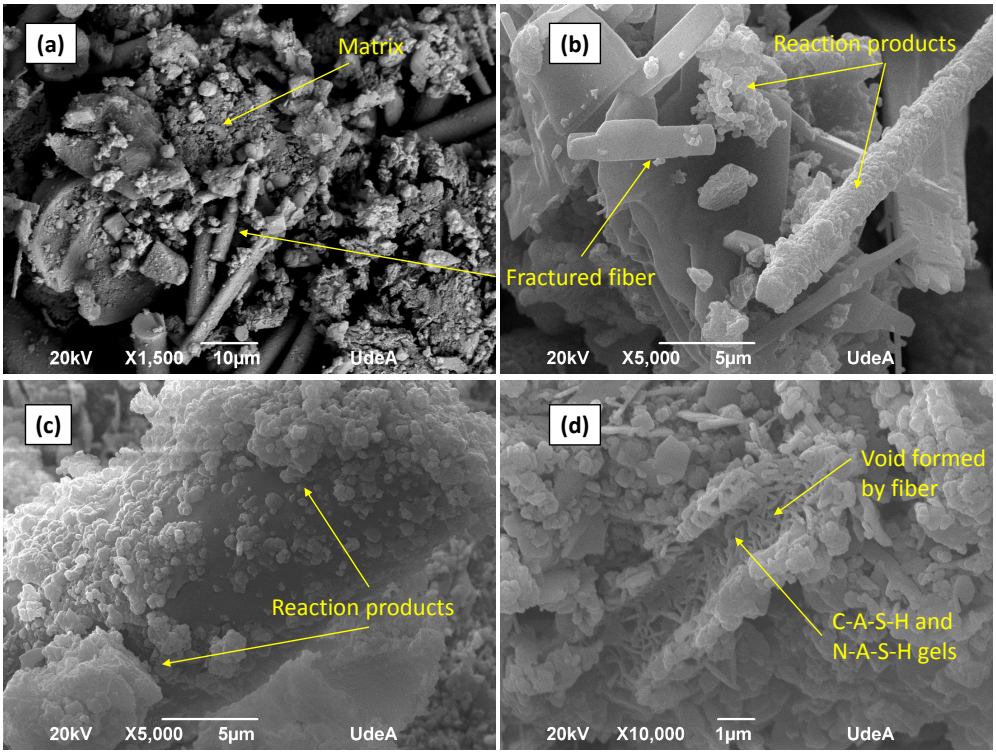

Figure 12. SEM images of alkali-activated cement combinations using Activator 1: (**a**) and (**b**) Act.1—0%, (**c**) Act.1—15% and (**d**) Act.1—30%.

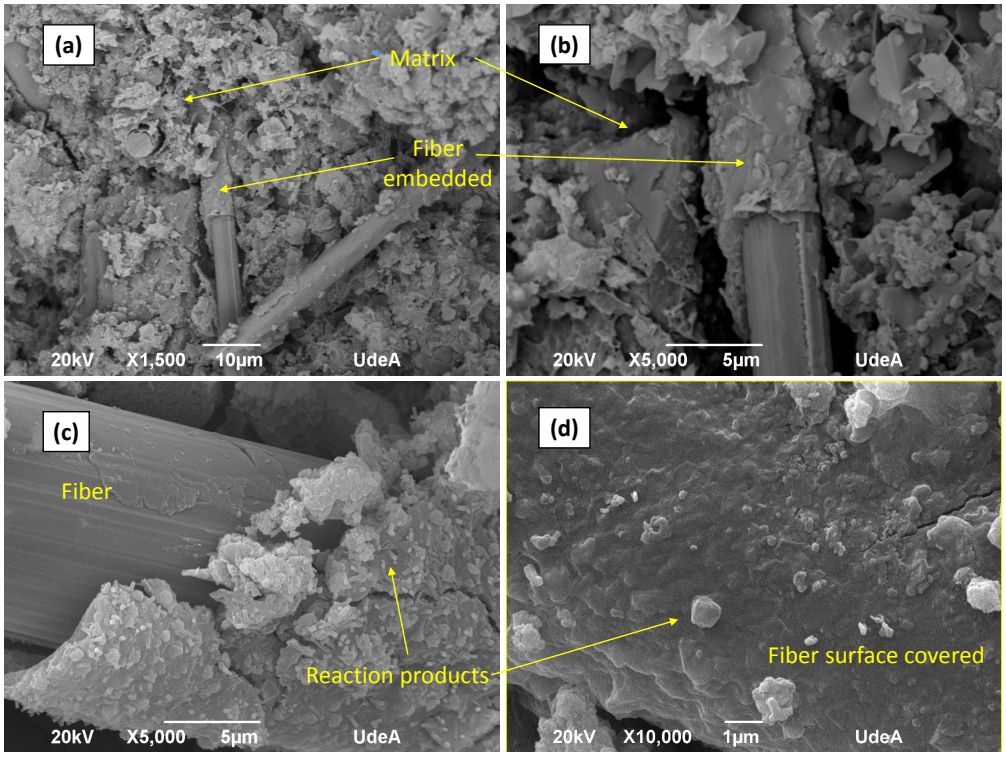

Figure 13. SEM images of alkali-activated cement combinations using Activator 2; (**a**) and (**b**) Act.2—0%; (**c**), Act.2—15%; (**d**) Act.2—30%.

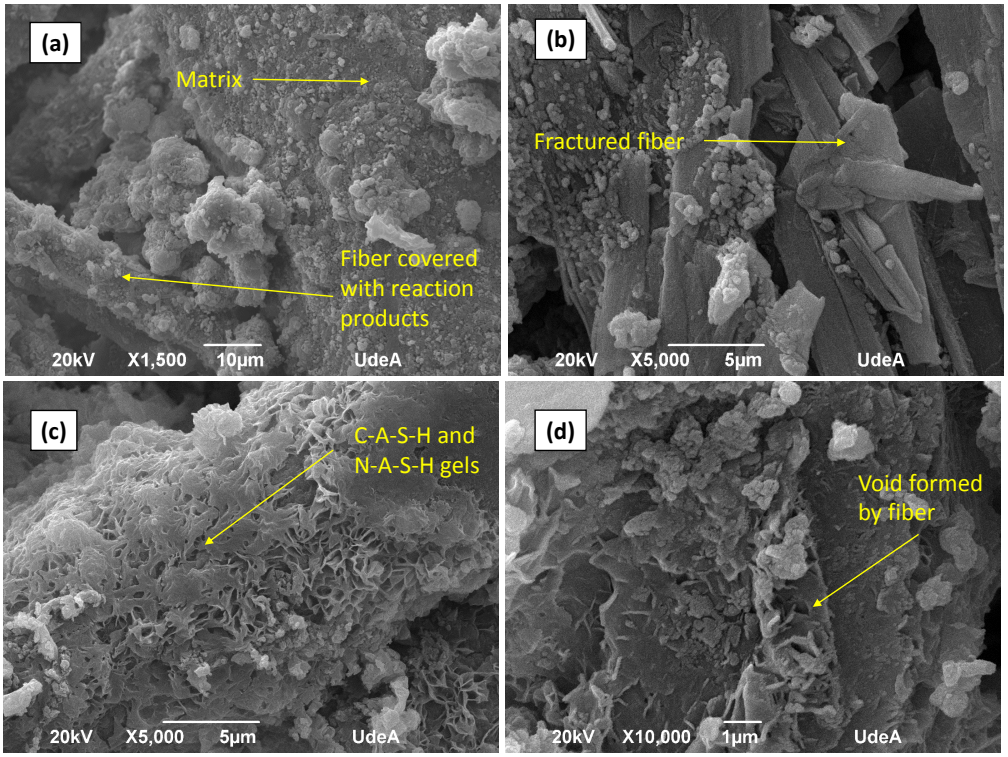

Figure 14. SEM images of alkali-activated cement combinations using Activator 3; (**a**) and (**b**) Act.3—0%; (**c**), Act.3—15% and (**d**) Act.3—30%.

Figures 15 and 16 show the EDS results of the samples with Act.1—0% and Act.3—0%, i.e., AAC. Based on the atomic percentages, an increase can be seen in Na from 7.82% to 14.48% in the AAC samples activated with Act.1 and with Act.3. Similarly, a slight increase in Al, from 8.06% to 10.37%, can be seen. The increase in the two elements is due to the increase in the Na:Al molar ratio between the two activators, which is 1.3 in the sample using Act.1 and 2.2 in the sample using Act.3. Therefore, it is confirmed through EDS analysis that the Na:Al molar ratio variable between Act.1 and Act.3 was effectively controlled.

In the case of Si, the content decreases from 15.96% in Act.1 to 13.93% in Act.3. Comparing the atomic contents with Act.1, the Si/Al ratio is found to be 1.98, very similar to the value defined in the experimental design. In contrast, with Act.3, this ratio decreased to 1.34. This is due to the variability of the atomic composition in the different phases formed, considering that the analysis is punctual.

Meanwhile, Figures 17 and 18 show the EDS results of the samples with Act.1-30% and Act.3—30%, i.e., AAHC samples with 30% OPC addition. Based on the atomic percentages and the spectra shown in the images, it can be seen that Ca is higher than in the alkali-activated cement shown in Figures 15 and 16. Specifically, the Ca percentage increases from 7.79% (Act.1—0% Figure 15), to 12.42% (Act.1—30%—Figure 17); and from 6.11% (Act.3—0%—Figure 16) to 13.35% (Act.3—30%—Figure 18). This increase is a result of the Ca content provided by the addition of OPC, which has a very active role in forming reaction products in the alkaline activation of SW.

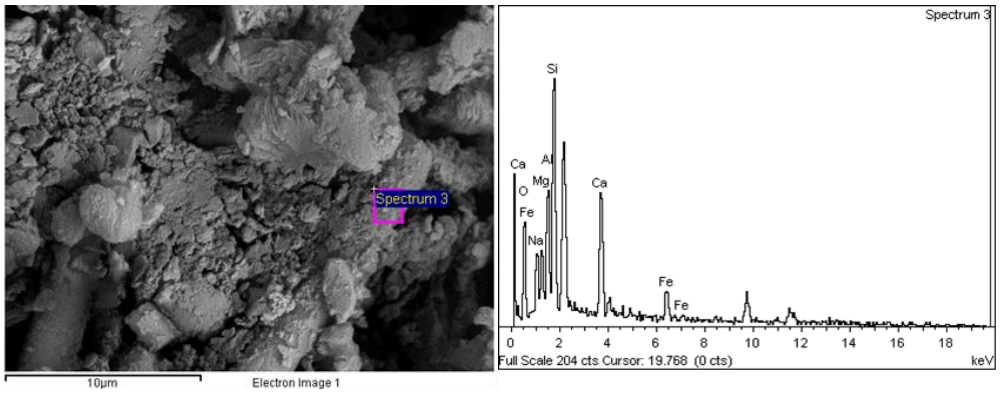

Element	Weight%	Atomic%
O K	36.19	51.95
Na K	7.83	7.82
Mg K	5.44	5.14
Al K	9.47	8.06
Si K	19.52	15.96
Ca K	13.59	7.79
Fe K	7.97	3.28
Totals	100.00	

Figure 15. EDS spectrum alkali-activated cement (Act.1—0%).

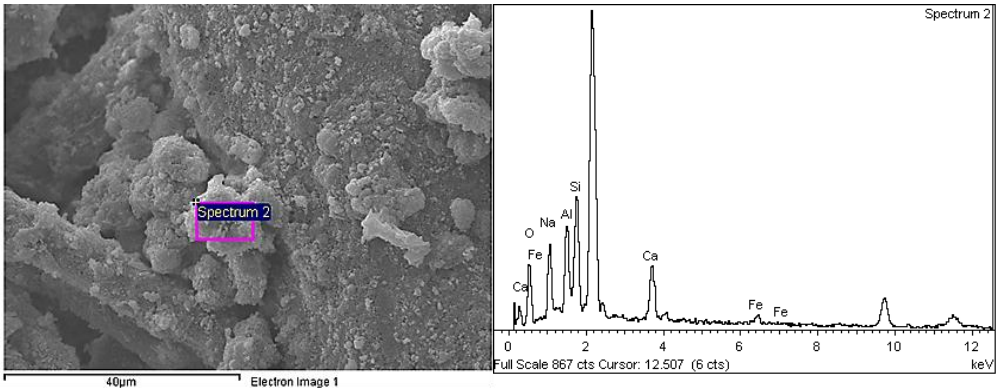

Element	Weight%	Atomic%
O K	38.93	53.45
Na K	15.16	14.48
Al K	12.74	10.37
Si K	17.80	13.93
Ca K	11.15	6.11
Fe K	4.22	1.66
Totals	100.00	

Figure 16. EDS spectrum alkali-activated cement (Act.3—0%).

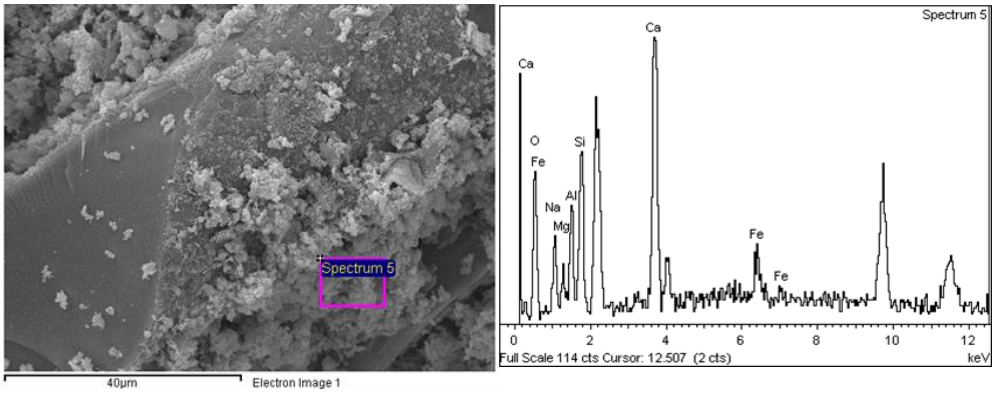

Element	Weight%	Atomic%
O K	43.95	61.84
Na K	7.33	7.18
Mg K	2.10	1.94
Al K	6.50	5.43
Si K	9.87	7.91
Ca K	22.12	12.42
Fe K	8.14	3.28
Totals	100.00	

Figure 17. EDS spectrum alkali-activated hybrid cement (Act.1—30%).

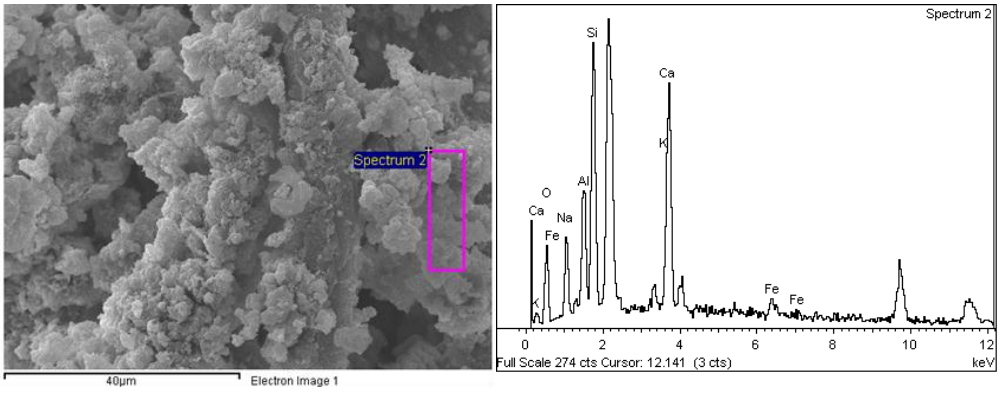

Element	Weight%	Atomic%
O K	34.24	50.51
Na K	9.03	9.27
Al K	8.71	7.62
Si K	19.59	16.46
K K	1.96	1.18
Ca K	22.68	13.35
Fe K	3.79	1.60
Totals	100.00	

Figure 18. EDS spectrum of alkali-activated cement (Act.3—30% activator).

4. Conslusions

Alkali-activated cement (AAC) and alkali-activated hybrid cement (AAHC) with the addition of OPC were obtained using $NaAlO_2$ and NaOH as an alkaline activator and mechanically and chemically evaluated. The following results were obtained:

Through a factorial design, it was shown that Act.1 (Na:Al = 1.3) and Act.2 (Na:Al = 1.8) significantly affects UCS at 28 days of curing. It also showed synergy between the activator and OPC factorial levels on UCS. Although Act.1 (Na:Al = 1.3) and Act.2 (Na:Al = 1.8) levels show a greater increment in strength; statistically, there was no significant difference between them. Similarly, it was established that the addition of OPC caused an increase in UCS, with maximum strength being reached at a level of 15% (12.3 MPa), using activator 2 (Act.2). At the maximum OPC level (30%), a decrease in UCS was observed with the use of Act.1 and Act.2. In contrast, with Act.3 the increase was very slight at both levels of OPC studied (15 and 30%).

Through XRD, N-A-S-H and C-A-S-H gels were identified in all the combinations, along with other products of the alkaline reaction, such as type-I C-S-H gel. Additionally, calcite, portlandite, hydrotalcite, and hydroandradite phases were identified. This last phase has not been reported in previous studies of alkali-activated systems with stone wool fiber and, as such, constitutes a novel finding. The characteristic peaks of Y-type zeolite were identified in the samples where Act.2 was used, while in the sample with Act.1, they were only observed slightly. The identification of this phase is associated with more significant development of N-A-S-H gel, which would explain the greater strength achieved with the use of Act.2. Similarly, the reduction in the strength or slight increase in it (in the case of the sample with Act. 3) when a level of 30% OPC was used in the AAHC samples can be explained by the excess Ca^{2+} ions in the system, which could favor more significant development of C-A-S-H gel than N-A-S-H gel.

Similarly, the morphology of reaction products, such as N-A-S-H and C-A-S-H, associated with forming a geopolymer could be observed through SEM. Additionally, it was confirmed through EDS that the Na:Al molar ratio could be controlled through the type of alkaline activator used.

Given the few antecedents found in the literature on alkaline activation of stone wool fiber to form hybrid cements, it can be stated that the findings of this work present a material that uses an industrial residue and relatively low quantities of OPC, with great potential for diverse applications and, above all, a lower environmental impact.

The use of AAC and AAHC as cementitious material is a valuable proposal for the circular economy in the construction sector, which simultaneously valorizes industrial waste from the thermal insulation sector and contributes to the fulfillment of Sustainable Development Goal 12 (SDG-12: Responsible Consumption and Production [60] related to substantially reduce waste generation through prevention, reduction, recycling, and reuse.

Author Contributions: Conceptualization, D.A.G.-O., M.A.G.-B., E.F.G.; methodology, D.A.G.-O., M.A.G.-B., E.F.G.; software, D.A.G.-O.; formal analysis, D.A.G.-O., M.A.G.-B., E.F.G.; writing—original draft preparation, D.A.G.-O., M.A.G.-B., E.F.G.; writing—review and editing, D.A.G.-O., M.A.G.-B., E.F.G. All authors have read and agreed to the published version of the manuscript.

Funding: This research has been funded by Universidad de Antioquia.

Institutional Review Board Statement: Not applicable.

Informed Consent Statement: Not applicable.

Data Availability Statement: All data generated or analysed during this study are within the submitted manuscript.

Acknowledgments: The authors are grateful for the valuable support provided by the Soil Mechanics Laboratory from the Universidad de Antioquia.

Conflicts of Interest: The authors declare no conflict of interest.

References

1. Pourakbar, S.; Huat, B.K. A review of alternatives traditional cementitious binders for engineering improvement of soils. *Int. J. Geotech. Eng.* **2016**, *6362*, 1–11. [CrossRef]
2. Pacheco-Torgal, F.; Abdollahnejad, Z.; Miraldo, S.; Kheradmand, M. Chapter 9 - Alkali-Activated Cement-Based Binders (AACBs) as Durable and Cost-Competitive Low-CO2 Binder Materials: Some Shortcomings That Need to be Addressed. In *Handbook of Low Carbon Concrete*; Nazari, A., Sanjayan, Eds.; Butterworth-Heinemann: Oxford, UK, 2017; pp. 195–216. [CrossRef]
3. Zhang, L. Production of bricks from waste materials—A review. *Constr. Build. Mater.* **2013**, *47*, 643–655. [CrossRef]
4. Davidovits, J. Properties of Geopolymer Cements. In Proceedings of the First International Conference on Alkaline Cements and Concretes, ResearchInstitute on Binders and Materials, Kiev State Technical University, Kiev, Ukraine, 11–14 October 1994; pp. 131–149.
5. Singh, B.; Ishwarya, G.; Gupta, M.; Bhattacharyya, S.K. Geopolymer concrete: A review of some recent developments. *Constr. Build. Mater.* **2015**, *85*, 78–90. [CrossRef]
6. Liew, Y.M.; Heah, C.Y.; Mohd Mustafa, A.B.; Kamarudin, H. Structure and properties of clay-based geopolymer cements: A review. *Prog. Mater. Sci.* **2016**, *83*, 595–629. [CrossRef]
7. McLellan, B.C.; Williams, R.P.; Lay, J.; Van Riessen, A.; Corder, G.D. Costs and carbon emissions for geopolymer pastes in comparison to ordinary portland cement. *J. Clean. Prod.* **2011**, *19*, 1080–1090. [CrossRef]
8. Abdollahnejad, Z.; Pacheco-Torgal, F.; Félix, T.; Tahri, W.; Barroso-Aguiar, J. Mix design, properties and cost analysis of fly ash-based geopolymer foam. *Constr Build Mater.* **2016**, *80*, 18–30. [CrossRef]
9. Mehta, A.; Siddique, R. An overview of geopolymers derived from industrial by-products. *Constr Build Mater.* **2016**, *127*, 183–198. [CrossRef]
10. Zhang, J.; Shi, C.; Zhang, Z.; Ou, Z. Durability of alkali-activated materials in aggressive environments: A review on recent studies. *Constr. Build Mater.* **2016**, *152*, 598–613. [CrossRef]
11. Amran, Y.H.M.; Alyousef, R.; Alabduljabbar, H.; El-Zeadani, M. Clean production and properties of geopolymer concrete: A review. *J. Clean. Prod.* **2020**, *251*, 119679. [CrossRef]
12. Luhar, S.; Nicolaides, D.; Luhar, I. Fire Resistance Behaviour of Geopolymer Concrete: An Overview. *Buildings* **2021**, *11*, 82. [CrossRef]
13. Sarıdemir, M.; Çelikten, S.; Ayaydın, G. Mechanical and microstructural properties of alkali-activated lightweight mortars exposed to high temperatures. *J. Build. Eng.* **2021**, *42*, 103050. [CrossRef]
14. Peng, K.D.; Huang, B.T.; Xu, L.Y.; Hu, R.L.; Dai, J.G. Flexural strengthening of reinforced concrete beams using geopolymer-bonded small-diameter CFRP bars. *Eng. Struct.* **2022**, *256*, 113992. [CrossRef]
15. Lao, J.C.; Xu, L.Y.; Huang, B.T.; Dai, J.G.; Shah, S.P. Strain-hardening Ultra-High-Performance Geopolymer Concrete (UHPGC): Matrix design and effect of steel fibers. *Compos. Commun.* **2022**, *30*, 101081. [CrossRef]
16. Vu, T.H.; Gowripalan, N. Mechanisms of heavy metal immobilisation using geopolymerisation techniques—A review. *J. Adv. Concr. Technol.* **2018**, *16*, 124–135. [CrossRef]
17. Li, Z.; Kondo, R.; Ikeda, K. Recycling of waste incineration bottom ash and heavy metal immobilization by geopolymer production. *J. Adv. Concr. Technol.* **2021**, *19*, 259–279. [CrossRef]
18. Shi, C.; Jiménez, A.F.; Palomo, A. New cements for the 21st century: The pursuit of an alternative to Portland cement. *Cement Concrete Res.* **2011**, *41*, 750–763. [CrossRef]
19. Provis, J.L.; Palomo, A.; Shi, C. Advances in understanding alkali-activated materials. *Cem. Concr. Res.* **2015**, *78*, 110–125. [CrossRef]
20. Palomo, A.; Monteiro, P.; Martauz, P.; Bilek, V.; Fernandez-Jimenez, A. Hybrid binders: A journey from the past to a sustainable future (opus caementicium futurum). *Cem. Concr. Res.* **2019**, *124*, 105829. [CrossRef]
21. Wang, W.; Noguchi, T. Alkali-silica reaction (ASR) in the alkali-activated cement (AAC) system: A state-of-the-art review. *Constr Build Mater.* **2020**, *252*, 119105. [CrossRef]
22. Xue, L.; Zhang, Z.; Wang, H. Hydration mechanisms and durability of hybrid alkaline cements (HACs): A review. *Constr Build Mater.* **2020**, *266*, 121039. [CrossRef]
23. García-Lodeiro, I.; Maltseva, O.; Palomo, Á.; Fernández-Jiménez, A. Cimenturi Hibride Alcaline. Partea I: Fundamente. *Rev. Romana Mater. Rom. J. Mater.* **2012**, *42*, 330–335.
24. Garcia-Lodeiro, I.; Palomo, A.; Fernández-Jiménez, A.; MacPhee, D. E. Compatibility studies between N-A-S-H and C-A-S-H gels. Study in the ternary diagram Na2O-CaO-Al2O3-SiO 2-H2O. *Cement Concrete Res.* **2011**, *41*, 923–931. [CrossRef]
25. Garcia-Lodeiro, I.; Fernandez-Jimenez, A.; Palomo, A. Hydration kinetics in hybrid binders: Early reaction stages. *Cem. Concr. Res.* **2011**, *39*, 82–92. [CrossRef]
26. Askarian, M.; Tao, Z.; Adam, G.; Samali, B. Mechanical properties of ambient cured one-part hybrid OPC-geopolymer concrete. *Constr Build Mater.* **2018**, *186*, 330–337. [CrossRef]
27. Palomo, A.; Maltseva, O.; Garcia-Lodeiro, I.; Fernandez-Jimenez, A. Hybrid Alkaline Cements. Part II: The Clinker Factor. *Rev. Romana Mater./ Rom. J. Mater.* **2013**, *43*, 74–80.
28. Xu, L.Y.; Qian, L.P.; Huang, B.T.; Dai, J.G. Development of artificial one-part geopolymer lightweight aggregates by crushing technique. *J. Clean. Prod.* **2021**, *315*, 128200. [CrossRef]
29. Sohn, J.L.; Kalbar, P.P.; Banta, G.T.; Birkved, M. Life-cycle based dynamic assessment of mineral wool insulation in a Danish residential building application. *J. Clean. Prod.* **2016**, *142*, 1–11. [CrossRef]

30. Väntsi, O.; Kärki, T.; Ka, T. Mineral wool waste in Europe: A review of mineral wool waste quantity, quality, and current recycling methods. *J. Mater. Cycles Waste Manag.* **2014**, *16*, 62–72. [CrossRef]
31. Yap, Z.S.; Khalid, N.H.A.; Haron, Z.; Mohamed, A.; Tahir, M. Waste MineralWool and Its Opportunities—A Review. *Materials* **2016**, *14*, 5777. [CrossRef]
32. Cheng, A. Lin, W.T.; Huang, R. Application of rock wool waste in cement-based composites. *Mater. Des.* **2011**, *32*, 636–642. [CrossRef]
33. Lin, W. T., Cheng, A., Huang, R. and Zou, S. Y. Improved microstructure of cement-based composites through the addition of rock wool particles. *Mater. Charact.* **2013**, *84*, 1–9. [CrossRef]
34. Stonys, R.; Kuznetsov, D.; Krasnikovs, A.; Skamat, J.; Baltakys, K.; Antonovic, V.; Cernasejus, O. Reuse of ultrafine mineral wool production waste in the manufacture of refractory concrete. *J. Environ. Manage.* **2016**, *176*, 149–156. [CrossRef]
35. Kubiliute, R.; Kaminskas, R.; Kazlauskaite, A. Mineral wool production waste as an additive for Portland cement. *Cem. Concr. Comp.* **2018**, *88*, 130–138. [CrossRef]
36. Medeiros, M.G.; Nadaleti, W.C.; Rocha, J.C.; Cheriaf, M.; Gleise, P.J.P.; de Castilhos, A.B. A cleaner material production by the incorporation of the rockwool waste into portland cement matrices. *J. Clean. Prod.* **2021**, *293*, 126059. [CrossRef]
37. Aymerich, F.; Fenu, L.; Meloni, P. Effect of reinforcing wool fibres on fracture and energy absorption properties of an earthen material. *Constr Build Mater.* **2012**, *27*, 66–72. [CrossRef]
38. Yliniemi, J.; Kinnunen, P.; Karinkanta, P.; Illikainen, M. Utilization of mineral wools as alkali-activated material precursor. *Materials* **2016**, *9*, 312. [CrossRef]
39. Gutiérrez, D.A.; Garcia, E.F.; Gomez, M.A. Mechanical and Physical Properties of Soil-Cement Blocks Reinforced with Mineral Wool and Sisal Fiber. *J. Mater. Civ. Eng.* **2017**, *29*, 1–12. [CrossRef]
40. Kinnunen, P.; Yliniemi, J.; Talling, B.; Illikainen, M. Rockwool waste in fly ash geopolymer composites. *J. Mater. Cycles Waste Manag.* **2017**, *19*, 1220–1227. [CrossRef]
41. Erofeev, V.T.; Rodin, A.I.; Yakunin, V.V.; Tuvin, M.N. Structure, composition and properties of geopolymers from mineral wool waste. *Mag. Civ. Eng.* **2019**, *90*, 3–14. [CrossRef]
42. Yliniemi, J.; Walkley, B.; Provis, J.L.; Kinnunen, P.; Illikainen, M. Influence of activator type on reaction kinetics, setting time, and compressive strength of alkali-activated mineral wools. *J. Therm. Anal. Calorim.* **2020**, *144*, 1129–1138. [CrossRef]
43. Pavlin, M.; Horvat, B.; Frankovič, A.; Ducman, V. Mechanical, microstructural and mineralogical evaluation of alkali-activated waste glass and stone wool. *Ceram. Int.* **2020**, *47*, 15102–15113. [CrossRef]
44. Norma TÉCNICA NTC colombiana 121. Cemento Portland. Especificaciones Físicas y Mecánicas. ICONTEC. Available online: https://www.academia.edu/39006642/NORMA_T%C3%89CNICA_NTC_COLOMBIANA_121 (accessed on 1 December 2022).
45. *ASTM C1157-08a*. Standard Performance Specification for Hydraulic Cement. American Society for Testing and Materials: West Conshohocken, PA, USA, 2011.
46. Duxson, P.; Provis, J.L.; Lukey, G.C.; Mallicoat, S.W.; Kriven, W.M.; Van Deventer, J.S.J. Understanding the relationship between geopolymer composition, microstructure and mechanical properties. *Colloids Surfaces A Physicochem. Eng. Asp.* **2005**, *269*, 47–58. [CrossRef]
47. Rodriguez, E.; De Gutierrez, R.M.; Bernal, S.; Gordillo, M. Effect of the SiO2/Al2O3 and Na2O/SiO2 ratios on the properties of geopolymers based on MK. *JRev. Fac. Ing. Univ. De Antioquia.* **2009**, *3*, 30–41.
48. Nazari, A.; Sanjayan, J.G. *Handbook of Low Carbon Concrete*, 1st ed.; Butterworth-Heinemann: Oxford, UK, 2017; 442p.
49. NFachinformationszentrum Chemie., N. I. of S. and T. U. S. (n.d.). "Inorganic Crystal Structure Database: ICSD. Inorganic Crystal Structure Database: ICSD. Karlsruhe." [Gaithersburg, MD]: Fachinformationszentrum; National Institute of Standards and Technology. Available online: https://icsd.fiz-karlsruhe.de/index.xhtml;jsessionid=CCE5475609E899ADEF9109776F390784 (accessed on 1 December 2022).
50. Yliniemi, J.; Laitinen, O.; Kinnunen P.; Illikainen, M. Pulverization of fibrous mineral wool waste. *J. Mater. Cycles Waste Manag.* **2017**, *20*, 1248–1256. [CrossRef]
51. Palomo, A.; Fernández-Jiménez, A.; Kovalchuk, G.; Ordoñez, L.M.; Naranjo, M.C. Opc-fly ash cementitious systems: Study of gel binders produced during alkaline hydration. *J. Mater. Sci.* **2007**, *42*, 2958–2966. [CrossRef]
52. Angulo-Ramírez, D.E.; Mejía de Gutiérrez, R.; Puertas, F. Alkali-activated Portland blast-furnace slag cement: Mechanical properties and hydration. *Constr Build Mater.* **2017**, *140*, 119–128. [CrossRef]
53. Lota, J.S.; Bensted, J.; Pratt, P.L. Effect of sodium aluminate on class G oil well cement hydration at low and ambient temperatures. In Proceedings of the 10th International Congress on the Chemistry of cement (p. Vol 3), Amarkai AB and Congrex, Gothenburg, Sweden, 2–6 June 1997.
54. Andersen, M.D.; Jakobsen, H.J.; Skibsted, J. Characterization of white Portland cement hydration and the C-S-H structure in the presence of sodium aluminate by 27Al and 29Si MAS NMR spectroscopy. *Cement Concrete Res.* **2004**, *34*, 857–868. [CrossRef]
55. Gutiérrez Pulido, H.; Vara Salazar, R.D.L. *Análisis y Diseño de Experimentos*, 3rd ed.; McGrawHill: Ciudad de México, Mexico, 2012.
56. Provis, J.L.; Lukey, G.C.; Van Deventer, J.S.J. Do geopolymers actually contain nanocrystalline zeolites? A reexamination of existing results. *Chem. Mater.* **2004**, *17*, 3075–3085. [CrossRef]
57. Garcia-Lodeiro, I.; Donatello, S.; Fernández-Jiménez, A.; Palomo, Á. Hydration of hybrid alkaline cement containing a very large proportion of fly ash: A descriptive model. *Materials* **2016**, *9*, 605. [CrossRef]

58. Luo, Y.; Jiang, Z.; Wang, D.; Lv, Y.; Gao, C.; Xue, G. Effects of alkaline activators on pore structure and mechanical properties of ultrafine metakaolin geopolymers cured at room temperature. *Const. Buil. Mater.* **2022**, *361*, 605. [CrossRef]
59. Phair, J.W.; Van Deventer, J.S.J. Characterization of fly-ash-based geopolymeric binders activated with sodium aluminate. *Ind. Eng. Chem. Res.* **2002**, *41*, 4242–4251. [CrossRef]
60. Organization of United Nations. Sustainable Development Goals (Goal 12: Ensure Sustainable Consumption and Production Patterns). 2022. Available online: Retrievedfromhttps://www.un.org/sustainabledevelopment/sustainable-consumption-production/ (accessed on 1 December 2022).